

Coordinated motion of epithelial layers on curved surfaces

L. Happel¹ and A. Voigt^{1,2,3}

¹*Institute of Scientific Computing, TU Dresden, 01062 Dresden, Germany*

²*Center for Systems Biology Dresden, Pfotenhauerstr. 108, 01307 Dresden, Germany*

³*Cluster of Excellence, Physics of Life, TU Dresden, Arnoldstr. 18, 01307 Dresden, Germany*

Coordinated cellular movements are key processes in tissue morphogenesis. Using a cell-based modeling approach we study the dynamics of epithelial layers lining surfaces with constant and varying curvature. We demonstrate that extrinsic curvature effects can explain the alignment of cell elongation with the principal directions of curvature. Together with specific self-propulsion mechanisms and cell-cell interactions this effect gets enhanced and can explain observed large-scale, persistent and circumferential rotation on cylindrical surfaces. On toroidal surfaces, extrinsic curvature only plays a minor role and the curvature coupling results primarily from intrinsic curvature. These findings unveil the role of curvature and postulate its importance for tissue morphogenesis.

Geometry, and in particular local curvature, influences biological systems at various length scales [47]. One example which is associated with curved epithelial layers is collective rotation. Persistent and synchronous rotation around a given axis of a sphere has been observed in vivo [3, 13, 17, 46, 50], in vitro [9, 20, 51, 54] and in silico [18, 50]. These phenomena differ significantly from collective behavior in flat space and are attributed to the geometric and topological properties of the sphere. Nevertheless, the underlying principles and mechanisms that trigger such collective rotation remain unclear even for surfaces as simple as a sphere, not to mention the curved environments that epithelial tissues encounter during morphogenesis. To better understand how curvature influences the mechanics of epithelial layers we consider cylindrical and toroidal surfaces. They provide ideal prototypical geometries to test the impact of curvature and allow for validation for specific cell types [14, 59].

At the single cell level it has been shown that cells sense and respond to curvature [1, 41, 58], essentially by regulating the transcellular network architecture [2, 7, 19] and aligning the filaments with the principal directions of curvature [7]. Experimental realizations furthermore show a dependence on the cell type, while, e.g., fibroblasts align with the minimal curvature direction [1, 7], MDCK cells align with the maximal curvature direction [7]. In addition to regulating the network architecture the nucleus also plays a role and cell migration on curved surfaces is shown to follow the path of least nuclear mechanical stress [41, 58]. These phenomena, which describe the response to cell-scale curvature, is termed curvotaxis [41] and can be extended to collective cell behavior on curved surfaces. Coordinated rotation has been associated with the alignment of filaments with principal directions of curvature, cell-cell adhesion as well as apical-basal polarity [51, 54]. In [14] cylindrical epithelia of MDCK cells are considered. The results indicate that proper cell-cell adhesion is essential, as well as aligned cellular polar order. This alignment is again in the principal directions of curvature. In contrast to these factors, the orientation of

the actin network does not seem to be essential for collective rotation. Also geometries with varying curvature, e.g. toroidal surfaces have been considered [59]. However, in this study only the cell elongation is addressed but not their coordinated motion.

In this Letter we propose a minimal cell-based surface model that reproduces these effects for MDCK cells. Two-dimensional vertex models, e.g., [6, 12, 42] and multi-phase field models [8, 24, 26, 28, 38, 39, 55] have been successfully used to simulate epithelial tissue in flat space. Extending these approaches to curved surfaces is still rare, see [49, 50] for vertex models and [18] for multi-phase field models considered on a sphere. None of these approaches account for extrinsic curvature contributions. These terms, which somehow translate the three-dimensional nature of a thin layer, for an epithelial layer, e.g. the difference between the apical and basal side, into an effectively two-dimensional framework on the curved surface, will be shown to be essential to model the effects of curvature discussed above. Extrinsic curvature effects are well established in the theory of surface liquid crystals [30, 31]. These theories force the director field to be tangential to the surface and the corresponding free energies contain coupling terms between the director field and the principal curvature directions of the shape operator [30, 31, 33, 37]. These terms follow naturally if the energies are derived as thin film limits from three-dimensional theories [15, 33, 37] and have shown various implications on phase transitions [35], active nematodynamic flows [4, 29, 32] and shape deformations [36]. However, in the context of cell alignment, these implications are unexplored.

We consider a multi-phase field model that allows for cell deformations and detailed cell-cell interactions, as well as extrinsic curvature coupling. To allow for large-scale tissue deformations local cellular rearrangements are required. These topological changes, e.g., T1 transitions or formation of rosettes, follow naturally in this framework [22, 55]. We consider two-dimensional phase field variables $\phi_i(\mathbf{x}, t)$ one for each cell, with \mathbf{x} defined on the surface \mathcal{S} . Values of $\phi_i = 1$ and $\phi_i = -1$ denote

the interior and exterior of a cell, respectively. The cell boundary is implicitly defined as the zero-level set of ϕ_i . We consider various surfaces \mathcal{S} , see Figure 1. They are topologically equivalent to a flat torus but differ by their geometric properties.

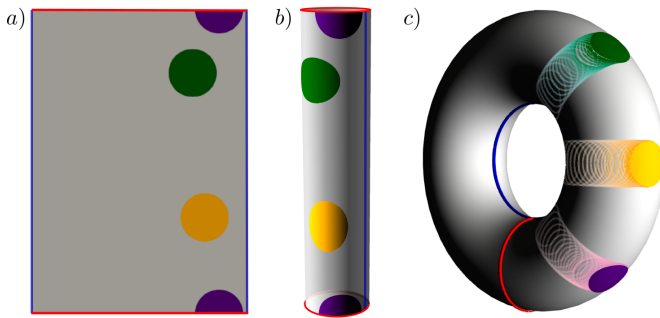


Figure 1. Considered geometries and resulting cell shapes. Red and blue lines mark periodic boundaries, which are glued together in b) and c) (not to scale). Three individual cells are shown in their equilibrium configuration in flat space a) and on a cylinder b). The colors correspond to the parameter Ec to account for the extrinsic curvature. $Ec = 0$ (purple) leads to a (geodesic) circle on both geometries. $Ec > 0$ (green) favours an alignment in the direction of the maximum absolute curvature and $Ec < 0$ (yellow) an alignment with the direction of minimal absolute curvature. The elongation is enhanced to be visible. On a toroidal surface the shape depends on the position. In c) the trajectories and the final positions and shapes of the cells are shown. The effect of extrinsic curvature is not visible in this case. All shapes are obtained by solving eq. (1) with $v_0 = 0$.

The dynamics for each ϕ_i are considered as

$$\partial_t \phi_i + v_0 (\mathbf{v}_i \cdot \nabla_S \phi_i) = \Delta_S \frac{\delta F}{\delta \phi_i}, \quad (1)$$

for $i = 1, \dots, N$, where N denotes the number of cells. F is a free energy and \mathbf{v}_i is a vector field used to incorporate active components, with a self-propulsion strength v_0 . The operators ∇_S and Δ_S denote the covariant derivative and Laplace-Beltrami operator on \mathcal{S} , respectively. All quantities are non-dimensional quantities. As in previous studies [18, 26, 27, 55–57], we consider conserved dynamics.

The free energy contains several contributions and reads $F = F_{CH} + F_{EC} + F_{INT}$ with a de Gennes-Cahn-Hilliard energy [5, 45]

$$F_{CH} = \sum_{i=1}^N \frac{1}{Ca} \int_S \frac{1}{G(\phi_i)} \left(\frac{\epsilon}{2} \|\nabla_S \phi_i\|^2 + \frac{1}{\epsilon} W(\phi_i) \right) dS,$$

which stabilizes the interface, with $W(\phi_i) = \frac{1}{4}(1 - \phi_i^2)^2$ a double-well potential, ϵ a small parameter determining the width of the diffuse interface and $1/G(\phi_i)$ called the de Gennes coefficient in polymer science. This term does not influence the asymptotic limit but helps to keep

$-1 \leq \phi_i \leq 1$, which becomes important as the numerical solution is more sensitive to variations as in flat space [5]. We consider $G(\phi_i) = \frac{3}{2}(1 - \phi_i^2)$. Ca is the capillary number. This covariant formulation only accounts for intrinsic curvature effects. Minimizing this energy by solving eq. (1) with $v_0 = 0$ on a cylindrical surface leads to a geodesic circle with no preferred orientation, see Figure 1 (purple cell). This does not resample the observed properties of single cells on cylindrical shapes [7].

Lets associate a director field with the shape of the cell. In flat space this has been considered in [28, 55]. Adapting the definition of the shape operator to the surface we obtain the surface Q-tensor fields

$$\mathbf{q}_i = \begin{pmatrix} \int_S \frac{(\partial_{\mathbf{t}_2} \phi_i)^2 - (\partial_{\mathbf{t}_1} \phi_i)^2}{2} dS & \int_S -\partial_{\mathbf{t}_1} \phi_i \partial_{\mathbf{t}_2} \phi_i dS \\ \int_S -\partial_{\mathbf{t}_1} \phi_i \partial_{\mathbf{t}_2} \phi_i dS & \int_S \frac{(\partial_{\mathbf{t}_1} \phi_i)^2 - (\partial_{\mathbf{t}_2} \phi_i)^2}{2} dS \end{pmatrix}$$

where \mathbf{t}_1 and \mathbf{t}_2 denote the directions of principal curvatures of the center of mass of cell i . Together with $\boldsymbol{\nu}$ the outward-pointing normal to the surface \mathcal{S} they define the Darboux frame, see SI for details. The eigenvectors of the tensor field \mathbf{q}_i correspond to the direction of largest elongation and contraction and the corresponding eigenvalues measure the degree of elongation and contraction in these directions. Using these directions to define director fields \mathbf{d}_i allows to associate nematic order to the epithelial tissue. This has been considered before in flat space [10, 28, 55] and on a sphere [18]. In our case \mathbf{q}_i and \mathbf{d}_i are tangential tensor and vector fields, respectively. Coarse-grained quantities of the surface Q-tensor fields \mathbf{q} and the director fields \mathbf{d} are considered in surface liquid crystal models. In these models both quantities are related by $\mathbf{q} = S(\mathbf{d} \otimes \mathbf{d} - \frac{1}{2}\mathbf{g})$ [35] where S is a nematic order parameter and \mathbf{g} is the metric of the surface \mathcal{S} . Already in typical one-constant approximations of the corresponding surface energies, if derived as a thin film limit from the corresponding 3D models, additional geometric coupling terms occur [30, 31, 33, 37]. In case of the surface Frank-Oseen model the term of interest reads

$$\|\nabla_C \mathbf{d}\|^2 = \|\nabla_S \mathbf{d}\|^2 + \langle \boldsymbol{\nu} \otimes \mathbf{B} \mathbf{d}, \boldsymbol{\nu} \otimes \mathbf{B} \mathbf{d} \rangle \quad (2)$$

where $\mathbf{B} = -\nabla_P \boldsymbol{\nu}$ denotes the shape operator and $\langle \cdot, \cdot \rangle$ the scalar product on \mathcal{S} [11]. In differential geometry ∇_C denotes the so-called Guenther derivative and ∇_P denotes the surface tangential gradient, see SI for definitions. There are various physical implications resulting from the choice of derivative, see [35] for an overview. Of relevance to our case is only the alignment of \mathbf{d} with principal directions of curvature resulting from the second summand in eq. (2). This coupling term has been added in an ad hoc manner in [4] to account for linear curvature contributions in surface active nematodynamics. Our goal is to account for this contribution in the cellular description. We therefore consider it in the phase

field context and define

$$F_{EC} = Ec \sum_{i=1}^N \int_{\mathcal{S}} \langle \boldsymbol{\nu} \otimes \mathbf{B} \nabla_{\mathcal{S}} \phi_i, \boldsymbol{\nu} \otimes \mathbf{B} \nabla_{\mathcal{S}} \phi_i \rangle d\mathcal{S}, \quad (3)$$

where Ec is a parameter that determines the preferred direction and strength of this geometric coupling. We furthermore use that the integral mean of $\nabla_{\mathcal{S}} \phi_i$ is orthogonal to the elongation of the cell and is thus related to \mathbf{d}_i . While F_{EC} can become negative, the area conservation of ϕ_i and F_{CH} guarantees a well-posed problem within reasonable parameter settings. Figure 1 shows the effect of F_{CH} and F_{EC} on a single cell on different geometries if $v_0 = 0$. While the shape is independent of the position in flat space and on the cylinders, with constant principle curvatures and zero Gaussian curvature, the shape depends on the position on the torus. Here F_{CH} can be reduced by moving the cell towards the region of maximal Gaussian curvature. The varying intrinsic curvature deforms the cell in an energetically favorable manner from elongation in toroidal direction in regions of lowest Gaussian curvature (inside) to elongation in poloidal direction in the region of highest Gaussian curvature (outside). The influence of F_{EC} is almost negligible in this setting. Further details on the evolution are provided in SI.

The missing energy contribution F_{INT} accounts for the interaction between cells. It is convenient to define $\psi_i = \frac{1}{2}(\phi_i + 1)$. A common way to model repulsive and attractive forces is to consider

$$F_{INT} = \sum_{i=1}^N \sum_{j \neq i} \int_{\mathcal{S}} \underbrace{a_{rep} \psi_i^2 \psi_j^2 - a_{att} \|\nabla_{\mathcal{S}} \psi_i\|^2 \|\nabla_{\mathcal{S}} \psi_j\|^2}_{:=f_{INT}} d\mathcal{S}$$

with coefficients a_{rep} and a_{att} , see [24, 40] for the corresponding form in flat space. We modify this formulation and consider the equilibrium condition $\frac{\epsilon}{2} \|\nabla_{\mathcal{S}} \phi_i\|^2 \approx \frac{1}{\epsilon} W(\phi_i)$ resulting from the tanh-profile of ϕ_i and approximate $a_{att} \|\nabla_{\mathcal{S}} \psi_i\|^2 \|\nabla_{\mathcal{S}} \psi_j\|^2 \approx \tilde{a}_{att} W(\phi_i) W(\phi_j)$, with the rescaled coefficient \tilde{a}_{att} . This leads to the numerically more appropriate form without derivatives, where

$$f_{INT} = \tilde{a}_{rep} (\phi_i + 1)^2 (\phi_j + 1)^2 - \tilde{a}_{att} (\phi_i^2 - 1)^2 (\phi_j^2 - 1)^2$$

with rescaled coefficients \tilde{a}_{rep} and \tilde{a}_{att} , as considered in [16, 21, 26, 48].

Activity is incorporated by self-propulsion defining \mathbf{v}_i . There are various possibilities, which differ by complexity, ranging from random motion [25] to considering mechanochemical subcellular processes [24, 27] and physical implications, e.g. polarity and velocity alignment and contact inhibition [53], see [55] for a comparison. Here we define $\mathbf{v}_i = v_0 (\cos(\theta_i) \mathbf{e}_1^i + \sin(\theta_i) \mathbf{e}_2^i)$ with v_0 a constant self-propulsion strength, the angle θ_i which is controlled by rotational noise $d\theta_i(t) = \sqrt{2D_r} dW_i(t)$ with

diffusivity D_r and a Wiener process W_i and the local orthonormal coordinate system $(\mathbf{e}_1^i, \mathbf{e}_2^i)$ in the tangent plane of the center of mass of cell i . We consider an elongation model with \mathbf{e}_1^i pointing in the direction of largest elongation, as considered in flat space in [28].

The problem can be solved numerically using surface finite elements [11, 34] and the parallelization concept introduced in [43], which considers each cell on a different core and accounts for the short-range interaction between cells to reduce the communication. This essentially allows scaling with the number of cells, see SI for details.

We consider three different cylindrical surfaces with equal surface area $|\mathcal{S}|$ but different curvature and 60 equally sized cells with a packing fraction of 90% placed on them with random initial direction of movement. For geometric quantities and detailed parameters see SI. Figure 2 shows data for one cylinder and $Ec > 0$, clearly indicating collective rotation, consistent with the experiments for MDCK cells in [14].

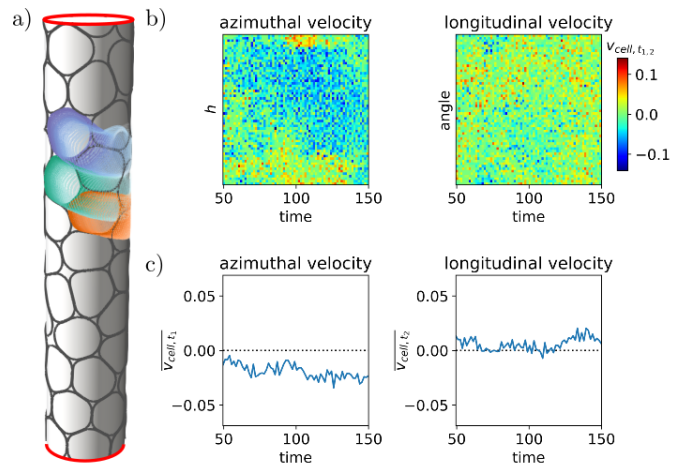


Figure 2. Evolution on a cylinder. a) Time instance of the evolution together with overlaid cell shapes ($\phi_i = 0$) and cells at previous time steps for three different cells. For corresponding movie see SI. b) and c) Kymographs and graphs displaying the average velocities of the cells from a) in azimuthal and longitudinal directions as a function of time.

All simulations on cylindrical surfaces are summarized in Figure 3. We consider each cell within a time frame after an initial phase and plot the distribution of their orientation and direction of movement with respect to the angle with the longitudinal direction for three different simulations, see SI for details on data analysis. The color coding corresponds to the magnitude of the averaged velocity. Without any extrinsic curvature contribution ($Ec = 0$ (purple cell), see Figure 3 (middle row)) there is no clear trend visible for any preferred direction of elongation or movement. For $Ec < 0$ (yellow cell) and $Ec > 0$ (green cell) the cells collectively elongate and move in the longitudinal and azimuthal di-

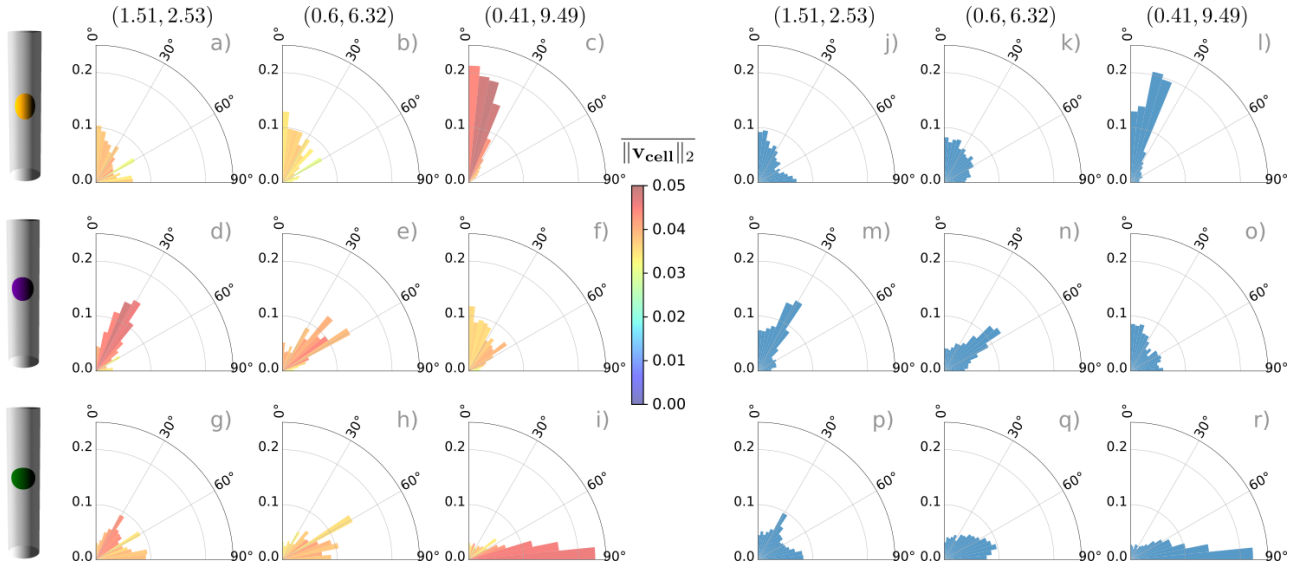


Figure 3. Distribution of direction of motion (left) and elongation direction (right) on three different cylindrical surfaces. The different rows correspond to the extrinsic curvature contribution $Ec < 0$, $Ec = 0$ and $Ec > 0$ from top to bottom. The columns show the different cylinders (r_{Cyl}, h_{Cyl}) with increasing curvature from left to right. The angle between \mathbf{e}_3 and the direction of movement or elongation direction is used as the angular coordinate and the ratio of cells with this property as the radial coordinate. *a)-i)* shows the direction of movement with color coding the mean velocity, *j)-r)* the direction of elongation. The data are the average over time and three simulations for each configuration.

rection, respectively. These effects are enhanced with increasing curvature. This is associated with stronger elongation, more pronounced movement in longitudinal or azimuthal direction and increased velocity, see Figure 3 (top and bottom row). The detailed data shown in Figure 2 corresponds to *h)*. Corresponding data for *a) - i)* are provided in SI. While the effect of extrinsic curvature is rather small for single cells, it is enhanced in coordinated motion leading qualitatively different behaviour. However, the enhancement of the elongation with principal curvature directions also strongly depends on the self-propulsion mechanism. Corresponding results for a random model, where \mathbf{e}_i^i is chosen as the direction of the velocity vector from the last time step, which can be considered as a generalization of active Brownian particles on surfaces to deformable objects [25], are shown in SI. This mechanism leads to a preferred elongation direction only for the cylindrical surfaces with the strongest curvature $(r_{Cyl}, h_{Cyl}) = (0.41, 9.49)$, but no tendency for collective motion in azimuthal or longitudinal direction.

On toroidal surfaces curvature varies along the poloidal direction, see SI. As already seen for a single cell, this has consequences for the shape and position of the cell. We consider the same setting on two different toroidal surfaces of equal area but now with 144 cells. Figure 4 shows a summary of the results. As in Figure 3 we plot the distribution of the direction of movement and the elongation direction. The angle is with respect to the poloidal direction. We see a strong elongation of the cells in the poloidal direction which is only slightly

increased (decreased) by the extrinsic curvature contribution if $Ec > 0$ ($Ec < 0$), respectively, see Figure 4 (top and bottom row). Considering the elongation as a function of the Gaussian curvature shows a clear tendency to change from elongation in toroidal direction towards poloidal direction going from negative to positive values. This agrees, at least qualitatively, with measurements for MDCK cells on toroidal surfaces within the region of negative Gaussian curvature [59]. Quantitative differences can be associated with significantly different numbers of cells and considered geometries, different measurement techniques and possible influences of the considered geometry in [59]. The direction of movement is less pronounced compared to cylindrical surfaces. This can be explained by geometric constraints, as movement in the poloidal direction is restricted by the geometry of the toroidal surface. However, as for single cells extrinsic curvature effects only play a minor role on toroidal surfaces.

Incorporating extrinsic curvature contributions into a cell-based surface multi-phase field model allows to effectively resolve the three-dimensional nature of epithelial layers, e.g., the difference between the apical and basal side. This reveals essential effects of curvature on single cells and their collective motion. The alignment of cells with the principal directions of curvature leads under appropriate propulsion mechanisms and cell-cell interactions to collective motion on specific geometries. On cylindrical surfaces this can lead to long-term changes from a quiescent state to spontaneous collective rotation,

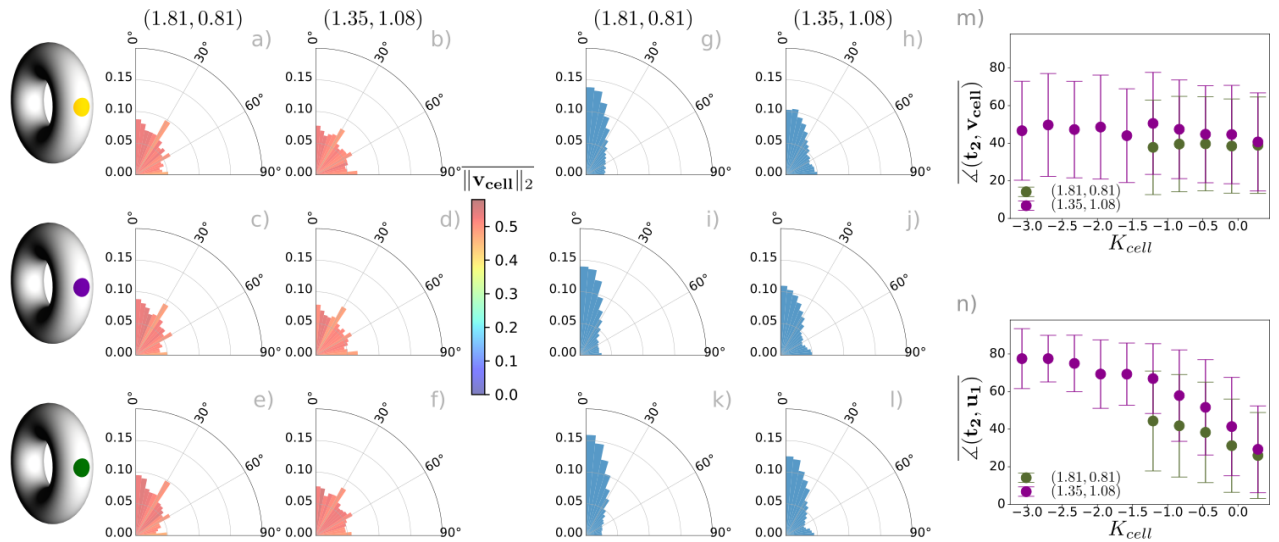


Figure 4. Distribution of direction of motion (left) and elongation direction (middle) on two different toroidal surfaces. The different rows correspond to the extrinsic curvature contribution $E_c < 0$, $E_c = 0$ and $E_c > 0$ from top to bottom. The columns show the different tori (R_T, r_T) . The angle between the poloidal direction and the direction of movement or elongation direction is used as the angular coordinate and the ratio of cells with this property as the radial coordinate. a)-f) shows the direction of movement with color coding the mean velocity, g)-l) the direction of elongation. The data are the average over time and three simulations for each configuration. (right) Angle of the direction of movement m) and elongation direction n) as function of the Gaussian curvature K of the toroidal surfaces averaged over the area of the cell.

as observed in vitro for MDCK cells [14]. Cylindrical surfaces are not only special mathematical objects, they are representative of many epithelial tissues, such as tubular vessels, ranging from small capillaries to large arteries, tubular glands, and ducts [1, 7]. On more general surfaces with varying Gaussian curvature these extrinsic curvature contributions only play a minor role. The curvature coupling is dominated by intrinsic curvature with a strong impact on the elongation of the cells. Both couplings vastly increase the range of tissue parameters to control the flow of the epithelial layer. Combining this with shape changes induced by these tangential flows, as considered in coarse-grained models for fluid deformable surfaces [23, 44, 52], has the potential to transform our understanding of morphogenesis.

Acknowledgments: This work was funded by DFG within FOR3013. We further acknowledge computing resources at FZ Jülich under grant PFAMDIS and at ZIH under grant WIR.

-
- [1] N. D. Bade, T. Xu, R. D. Kamien, R. K. Assoian, and K. J. Stebe. Gaussian curvature directs stress fiber orientation and cell migration. *Biophys. J.*, 114:1467–1476, 2018.
- [2] D. Baptista, L. Teixeira, C. van Blitterswijk, S. Giseler, and R. Truckenmüller. Overlooked? Underestimated? Effects of substrate curvature on cell behavior. *Trends in Biotechnology*, 37:838–854, 2019.

- [3] K. Barlan, M. Cetera, and S. Horne-Badovinac. Fat2 and Lar define a basally localized planar signaling system controlling collective cell migration. *Developmental Cell*, 40:467–477, 2017.
- [4] S. Bell, S.-Z. Lin, J.-F. Rupprecht, and J. Prost. Active nematic flows over curved surfaces. *Phys. Rev. Lett.*, 129:118001, 2022.
- [5] M. Benes, M. Kolar, J. M. Sischka, and A. Voigt. Degenerate area preserving surface Allen-Cahn equation and its sharp interface limit. *arXiv:2303.04018*, 2023.
- [6] D. Bi, X. Yang, M. C. Marchetti, and M. L. Manning. Motility-driven glass and jamming transitions in biological tissues. *Phys. Rev. X*, 6:021011, 2016.
- [7] S. J. P. Callens, R. J. C. Uyttendaele, L. E. Fratila-Apachitei, and A. A. Zadpoor. Substrate curvature as a cue to guide spatiotemporal cell and tissue organization. *Biomaterials*, 232:119739, 2020.
- [8] B. A. Camley, Y. Zhang, Y. Zhao, B. Li, E. Ben-Jacob, H. Levine, and W.-J. Rappel. Polarity mechanisms such as contact inhibition of locomotion regulate persistent rotational motion of mammalian cells on micropatterns. *Proc. Nat. Acad. Sci. (USA)*, 111:14770–14775, 2014.
- [9] A. S. Chin, K. E. Worley, P. Ray, G. Kaur, J. Fan, and L. Q. Wan. Epithelial cell chirality revealed by three-dimensional spontaneous rotation. *Proc. Nat. Acad. Sci. (USA)*, 115:12188–12193, 2018.
- [10] A. Doostmohammadi, J. Ignes-Mullol, J. M. Yeomans, and F. Sagues. Active nematics. *Nature Commun.*, 9:3246, 2018.
- [11] G. Dziuk and C. M. Elliott. Finite element methods for surface PDEs. *Acta Numerica*, 22:289–396, 2013.
- [12] R. Farhadifar, J.-C. Roper, B. Algouy, S. Eaton, and F. Jülicher. The influence of cell mechanics, cell-cell interactions, and proliferation on epithelial packing. *Cur-*

- rent Biology*, 17:2095–2104, 2007.
- [13] P. A. Fernandez, B. Buchmann, A. Goychuk, L. K. Engelbrecht, M. K. Raich, C. H. Scheel, E. Frey, and A. R. Bausch. Surface-tension-induced budding drives alveologenesis in human mammary gland organoids. *Nature Physics*, 17:1130–1136, 2021.
- [14] A. Glentis, C. Blanch-Mercader, L. Balasubramaniam, T.B. Saw, J. d’Alessandro, S. Janel, A. Douanier, B. Delaval, F. Lafont, C. T. Lim, D. Delacour, J. Prost, W. Xi, and B. Ladoux. The emergence of spontaneous coordinated epithelial rotation on cylindrical curved surfaces. *Sci. Adv.*, 8:eabn5406, 2022.
- [15] D. Golovaty, J. Alberto Montero, and P. Sternberg. Dimension reduction for the Landau-de Gennes model on curved nematic thin films. *J. Nonlin. Sci.*, 27:1905–1932, 2017.
- [16] R. Gu, X. Wang, and M. Gunzburger. Simulating vesicle-substrate adhesion using two phase field functions. *J. Comput. Phys.*, 275:626–641, 2014.
- [17] S. L. Haigo and D. Bilder. Global tissue revolutions in a morphogenetic movement controlling elongation. *Science*, 331:1071–1074, 2011.
- [18] L. Happel, D. Wenzel, and A. Voigt. Effects of curvature on epithelial tissue - coordinated rotational movement and other spatiotemporal arrangements. *Europhys. Lett.*, 138:67002, 2022.
- [19] N. Harmand, A. Huang, and S. Henon. 3D shape of epithelial cells on curved substrates. *Phys. Rev. X*, 11:031028, 2021.
- [20] E. Hirata, T. Ichikawa, S.-I. Horike, and E. Kiyokawa. Active K-RAS induces the coherent rotation of epithelial cells: A model for collective cell invasion in vitro. *Cancer Sci.*, 109:4045–4055, 2018.
- [21] H. P. Jain, D. Wenzel, and A. Voigt. Impact of contact inhibition on collective cell migration and proliferation. *Phys. Rev. E*, 105:034402, 2022.
- [22] H. P. Jain, A. Voigt, and L. Angheluta. Robust statistical properties of T1 transitions in a multi-phase field model of cell monolayers. *Sci. Rep.*, 13:10096, 2023.
- [23] V. Krause and A. Voigt. A numerical approach for fluid deformable surfaces with conserved enclosed volume. *J. Comput. Phys.*, 486:112097, 2023.
- [24] J. Loeber, F. Ziebert, and I. S. Aranson. Collisions of deformable cells lead to collective migration. *Sci. Rep.*, 5:9172, 2015.
- [25] B. Loewe, M. Chiang, D. Marenduzzo, and M. C. Marchetti. Solid-liquid transition of deformable and overlapping active particles. *Phys. Rev. Lett.*, 125:038003, 2020.
- [26] W. Marth and A. Voigt. Collective migration under hydrodynamic interactions: a computational approach. *Interf. Focus*, 6:20160037, 2016.
- [27] W. Marth, S. Praetorius, and A. Voigt. A mechanism for cell motility by active polar gels. *J. Roy. Soc. Interf.*, 12:20150161, 2015.
- [28] R. Mueller, J. M. Yeomans, and A. Doostmohammadi. Emergence of active nematic behavior in monolayers of isotropic cells. *Phys. Rev. Lett.*, 122:048004, 2019.
- [29] G. Napoli and S. Turzi. Spontaneous helical flows in active nematics lying on a cylindrical surface. *Phys. Rev. E*, 101:022701, 2020.
- [30] G. Napoli and L. Vergori. Surface free energies for nematic shells. *Phys. Rev. E*, 85:061701, 2012.
- [31] G. Napoli and L. Vergori. Extrinsic curvature effects on nematic shells. *Phys. Rev. Lett.*, 108:207803, 2012.
- [32] M. Nestler and A. Voigt. Active nematodynamics on curved surfaces—the influence of geometric forces on motion patterns of topological defects. *Commun. Comput. Phys.*, 31:947–965, 2022.
- [33] M. Nestler, I. Nitschke, S. Praetorius, and A. Voigt. Orientational order on surfaces: The coupling of topology, geometry, and dynamics. *J. Nonlin. Sci.*, 28:147–191, 2018.
- [34] M. Nestler, I. Nitschke, and A. Voigt. A finite element approach for vector-and tensor-valued surface PDEs. *J. Comput. Phys.*, 389:48–61, 2019.
- [35] M. Nestler, I. Nitschke, H. Löwen, and A. Voigt. Properties of surface Landau-de Gennes Q-tensor models. *Soft Matter*, 16:4032–4042, 2020.
- [36] I. Nitschke, S. Reuther, and A. Voigt. Liquid crystals on deformable surfaces. *Proc. Roy. Soc. A*, 476:20200313, 2020.
- [37] I. Nitschke, M. Nestler, S. Praetorius, H. Löwen, and A. Voigt. Nematic liquid crystals on curved surfaces: a thin film limit. *Proc. Roy. Soc. A*, 474:20170686, 2018.
- [38] M. Nonomura. Study on multicellular systems using a phase field model. *PLoS ONE*, 7:e33501, 2012.
- [39] B. Palmieri, Y. Bresler, D. Wirtz, and M. Grant. Multiple scale model for cell migration in monolayers: Elastic mismatch between cells enhances motility. *Sci. Rep.*, 5:11745, 2015.
- [40] G. Peyret, R. Mueller, J. d’Alessandro, S. Begnaud, P. Marcq, R.-M. Mège, J. M. Yeomans, A. Doostmohammadi, and B. Ladoux. Sustained oscillations of epithelial cell sheets. *Biophys. J.*, 117:464–478, 2019.
- [41] L. Pieuchot, J. Marteau, A. Guignandon, T. Dos Santos, B. Isabelle, P. Chauvy, T. Cloatre, A. Ponche, T. Petithory, P. Rougerie, M. Vassaux, J.-L. Milan, N. Wakhloo, A. Spangenberg, M. Bigerelle, and K. Anselme. Curvotaxis directs cell migration through cell-scale curvature landscapes. *Nature Commun.*, 9:3995, 2018.
- [42] M. Popovic, V. Druelle, N. A. Dye, F. Juelicher, and M. Wyart. Inferring the flow properties of epithelial tissues from their geometry. *New J. Phys.*, 23:033004, 2021.
- [43] S. Praetorius and A. Voigt. Collective cell behavior - a cell-based parallelization approach for a phase field active polar gel model. In K. Binder, M. Müller, and A. Trautmann, editors, *NIC Symposium 2018*, volume 49, pages 369–376, Jülich, 2018. Forschungszentrum Jülich GmbH, Zentralbibliothek.
- [44] S. Reuther, I. Nitschke, and A. Voigt. A numerical approach for fluid deformable surfaces. *J. Fluid Mech.*, 900:R8, 2020.
- [45] M. Salvalaglio, A. Voigt, and S. M. Wise. Doubly degenerate diffuse interface models of surface diffusion. *Math. Meth. Appl. Sci.*, 44:5385–5405, 2021.
- [46] K. Sato, T. Hiraiwa, E. Maekawa, A. Isomura, T. Shibata, and E. Kuranaga. Left–right asymmetric cell intercalation drives directional collective cell movement in epithelial morphogenesis. *Nature Commun.*, 6:10074, 2015.
- [47] B. Schamberger, R. Ziege, K. Anselme, M. Ben Amar, M. Bykowski, André P. G. Castro, A. Cipitria, R. A. Coles, R. Dimova, M. Eder, S. Ehrig, L. M. Escudero, M. E. Evans, P. R. Fernandes, P. Fratzl, L. Geris, N. Gierlinger, E. Hannezo, A. Igljč, J. J. K. Kirkensgaard, P. Kollmannsberger, L. Kowalewska, N. A. Kurniawan, I. Papantoniou, L. Pieuchot, T. H. V. Pires, L. D. Ren-

- ner, A. O. Sageman-Furnas, G. E. Schröder-Turk, A. Sengupta, V. R. Sharma, A. Tagua, C. Tomba, X. Trepát, S. L. Waters, E. F. Yeo, A. Roschger, C. M. Bidan, and J. W. C. Dunlop. Curvature in biological systems: Its quantification, emergence, and implications across the scales. *Adv. Materials*, 35:2206110, 2022.
- [48] L. Shen, P. Lin, Z. Xu, and S. Xu. Thermodynamically consistent diffuse interface model for cell adhesion and aggregation. *arXiv:2205.07190*, 2022.
- [49] D. M. Sussman. Interplay of curvature and rigidity in shape-based models of confluent tissue. *Phys. Rev. Research*, 2:023417, 2020.
- [50] T. H. Tan, A. Amiri, I. Seijo-Barandiarán, M. F. Staddon, A. Materne, S. Tomas, C. Duclut, M. Popović, A. Grapin-Botton, and F. Jülicher. Emergent chirality in active solid rotation of pancreas spheres. *bioRxiv*, 2022. doi:10.1101/2022.09.29.510101.
- [51] K. Tanner, H. Mori, R. Mroue, A. Bruni-Cardoso, and M. J. Bissell. Coherent angular motion in the establishment of multicellular architecture of glandular tissues. *Proc. Nat. Acad. Sci. (USA)*, 109:1973–1978, 2012.
- [52] A. Torres-Sánchez, D. Millán, and M. Arroyo. Modelling fluid deformable surfaces with an emphasis on biological interfaces. *J. Fluid Mech.*, 872:218–271, 2019.
- [53] E. Vercuryse, D. B. Brückner, M. Gómez-González, M. Luciano, Y. Kalukula, L. Rossetti, X. Trepát, E. Hannezo, and S. Gabriele. Geometry-driven migration efficiency of minimal cell clusters. *bioRxiv*, 2022. doi:10.1101/2022.07.17.500364.
- [54] H. Wang, S. Lacoche, L. Huang, B. Xue, and S. K. Muthuswamy. Rotational motion during three-dimensional morphogenesis of mammary epithelial acini relates to laminin matrix assembly. *Proc. Nat. Acad. Sci. (USA)*, 110:163–168, 2013.
- [55] D. Wenzel and A Voigt. Multiphase field models for collective cell migration. *Phys. Rev. E*, 184:054410, 2021.
- [56] D. Wenzel, S. Praetorius, and A. Voigt. Topological and geometrical quantities in active cellular structures. *J. Chem. Phys.*, 150:164108, 2019.
- [57] D. Wenzel, M. Nestler, S. Reuther, M. Simon, and A. Voigt. Defects in active nematics - algorithms for identification and tracking. *Comput. Meth. Appl. Math.*, 21:683–692, 2021.
- [58] M. Werner, A. Petersen, N. A. Kurniawan, and C. V. C. Bouten. Cell-perceived substrate curvature dynamically coordinates the direction, speed, and persistence of stromal cell migration. *Adv. Biosystems*, 3:1900080, 2019.
- [59] S.-M. Yu, B. Li, F. Amblard, S. Granick, and Y.-K. Cho. Adaptive architecture and mechanoresponse of epithelial cells on a torus. *Biomaterials*, 265:120420, 2021.

SUPPLEMENTAL MATERIAL

Coordinated motion of epithelial layers on curved surfaces

L. Happel,¹A. Voigt,^{1,2,3}

¹*Institute of Scientific Computing, TU Dresden, 01062 Dresden, Germany*

²*Center for Systems Biology Dresden, Pfotenhauerstr. 108, 01307 Dresden, Germany*

³*Cluster of Excellence, Physics of Life, TU Dresden, Arnoldstr. 18, 01307 Dresden, Germany*

GEOMETRY

We consider two prototypical geometries, cylindrical and toroidal surfaces. With periodic boundary conditions these geometries are topologically equivalent to a flat torus but differ in their geometric properties. Figure S1 shows the principal directions of curvature for these geometries. Cylindrical surfaces are characterized by their radius r_{Cyl}

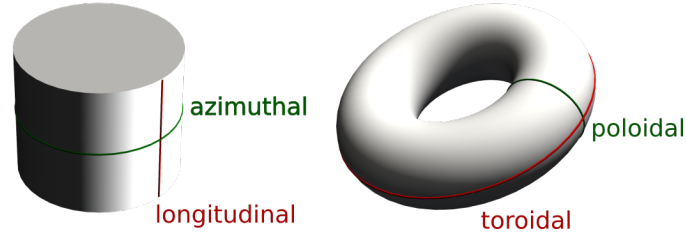


Figure S1. Principal directions of curvature. a) for cylindrical and b) for toroidal surfaces.

and height h_{Cyl} , see Figure S2. They are labeled as (r_{Cyl}, h_{Cyl}) . The principal curvatures are $k_1 = 1/r_{Cyl}$ and $k_2 = 0$, corresponding to the azimuthal and longitudinal direction, respectively. The three cylindrical shapes have the same area $|\mathcal{S}| = 2\pi r_{Cyl} h_{Cyl}$. Toroidal surfaces are characterized by two radii R_T and r_T , see Figure S3. They are labeled

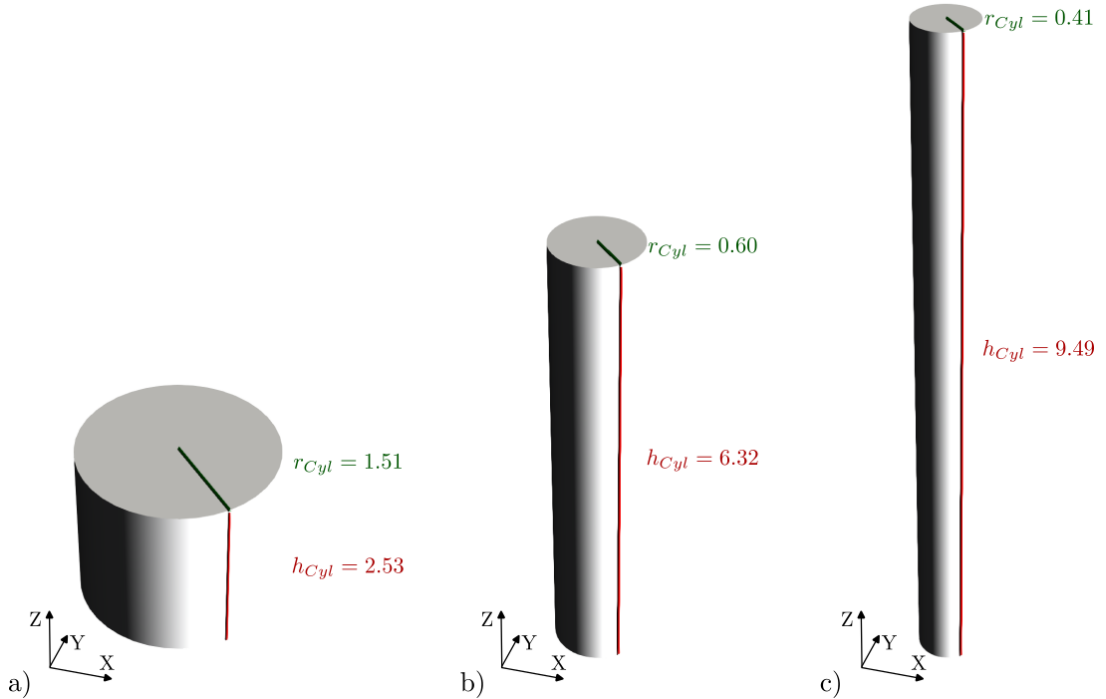


Figure S2. Cylindrical surfaces used for the simulations with corresponding values (r_{Cyl}, h_{Cyl}) .

as (R_T, r_T) . The principal curvatures are $k_1 = (\sqrt{x_1^2 + x_2^2} - R_T)/r_T$ in toroidal direction and $k_2 = 1/r_T$ in poloidal

direction. The two toroidal shapes have the same area $|\mathcal{S}| = 4\pi^2 R_T r_T$. However, they strongly differ with respect to the Gaussian curvature $K = k_1 k_2$.

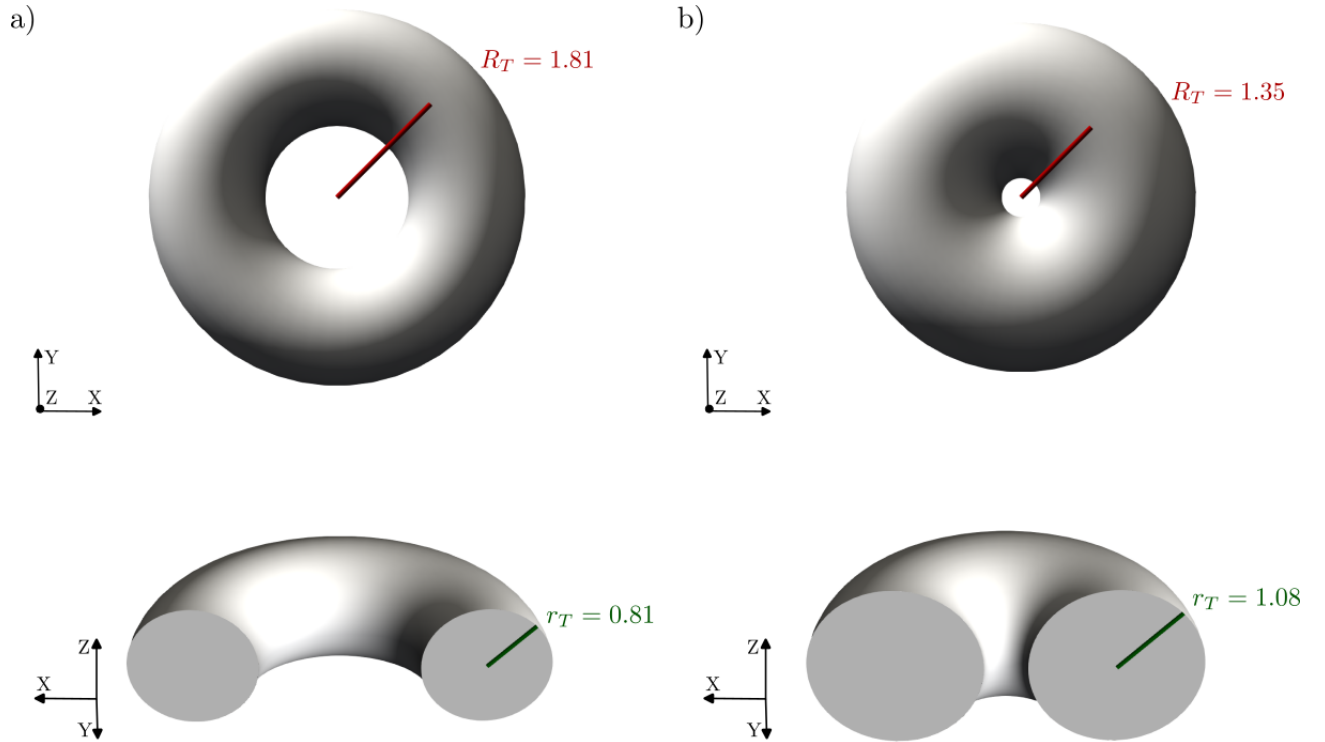


Figure S3. Toroidal surfaces used for the simulations with corresponding values (R_T, r_T) .

DIFFERENTIAL GEOMETRY

Related to the surface \mathcal{S} we denote the outward pointing surface normal $\boldsymbol{\nu}$, the shape operator (negative of the extended Weingarten map) \mathbf{B} with $\mathbf{B} = -\nabla_P \boldsymbol{\nu}$ and the surface projection $\mathbf{P} = \mathbf{I} - \boldsymbol{\nu} \otimes \boldsymbol{\nu}$. Let $\nabla_{\mathcal{S}}$ be the covariant derivative. This operator is well defined for vector fields in the tangent bundle of \mathcal{S} . For the tangential director field \mathbf{d} we use the Guenther derivative, which is a component-wise tangential derivative defined as $\nabla_C \mathbf{d} = (\nabla \mathbf{d}^e)|_{\mathcal{S}} \mathbf{P}$ where \mathbf{d}^e is an extension of \mathbf{d} constant in normal direction and ∇ is the gradient of the embedding space \mathbb{R}^3 . For tangential director fields ∇_C relates to the covariant derivative $\nabla_{\mathcal{S}}$ by $\nabla_C \mathbf{d} = \nabla_{\mathcal{S}} \mathbf{d} + \boldsymbol{\nu} \otimes \mathbf{B} \mathbf{d}$, see [S1, S4, S7]. For sufficiently smooth \mathbb{R}^3 -vector fields \mathbf{w} the tangential derivative ∇_P is defined as $\nabla_P \mathbf{w} = \mathbf{P} \nabla \mathbf{w}^e \mathbf{P}$. Again, \mathbf{w}^e is an extension of \mathbf{w} constant in normal direction. For scalar fields these derivatives are identical, e.g. $\nabla_{\mathcal{S}} \phi = \nabla_C \phi = \nabla_P \phi$.

NUMERICAL ISSUES

The resulting system of surface partial differential equations is solved by surface finite elements [S5, S9] within the toolbox AMDiS [S12, S14] which was recently integrated into the DUNE framework [S3]. For the surface discretization an analytic grid function from DUNE-CurvedGrid [S10] is used, which gives access to analytic formulas for the projection \mathbf{P} , surface normal $\boldsymbol{\nu}$ and the shape operator \mathbf{B} . An accurate representation of the surface is crucial as F_{EC} has been shown to be sensitive to surface discretization errors.

Each cell, represented by the phase field variable ϕ_i , is considered on its own core and has its own mesh, which is adaptively refined within the diffuse interface to ensure approximately 7 grid points across the interface. Dealing with F_{INT} leads to a non-local problem and in principle requires communication between all cells and thus all cores. Due to the short-range interaction this communication can be reduced to the neighboring cells. This approach allows parallel scaling with the number of cells [S11], which has been demonstrated for up to 1,000 cells in flat space and carries over to the curved surface.

We split the higher order partial differential equations for each ϕ_i into a system of second order partial differential equations by introducing $\mu_i = \frac{\delta F}{\delta \phi_i}$ and consider P^2 -Lagrange elements for the unknowns ϕ_i and μ_i .

Discretization in time is done by finite differences using

$$\partial_t \phi_i \approx \frac{\phi_i^{n+1} - \phi_i^n}{\tau_n},$$

where τ_n denotes the time step size for the n -th time step. It is chosen to fulfill the CFL condition. In general a linear implicit-explicit scheme is used, where all linear terms are treated implicitly and all nonlinear terms explicitly. However, the double-well potential $W(\phi_i)$ and the non-linear terms in F_{INT} are linearized with one Newton-step and the de Gennes factor $G(\phi_i)$ is regularized by

$$G_\eta(\phi_i) = \sqrt{\frac{9}{4}(1 - \phi_i^2)^2 + \eta^2 \epsilon^2}, \quad (\text{S1})$$

with $\eta > 0$. The resulting linear system in each time step is solved by the direct solver UMFPACK.

To extract the elongation of the cells the eigenvalues and eigenvectors of the surface Q-tensors \mathbf{q}_i have to be computed. It turns out to be essential that these surface Q-tensors are defined with respect to the local coordinate system of the tangent plane at the center of mass. The Darboux frame with \mathbf{t}_1 and \mathbf{t}_2 the directions of the principal curvatures and $\boldsymbol{\nu}$ the outward-pointing normal to the surface \mathcal{S} at this point is needed to resolve the sensitive dependence on curvature. We calculate the eigenvalues of \mathbf{q}_i as

$$\begin{aligned} \lambda_i^1 &= \sqrt{\left(\int_{\mathcal{S}} \frac{1}{2} ((\partial_{\mathbf{t}_2} \phi_i)^2 - (\partial_{\mathbf{t}_1} \phi_i)^2) d\mathcal{S} \right)^2 + \left(\int_{\mathcal{S}} -\partial_{\mathbf{t}_1} \phi_i \partial_{\mathbf{t}_2} \phi_i d\mathcal{S} \right)^2} \\ \lambda_i^2 &= -\lambda_i^1 \end{aligned}$$

and the corresponding eigenvectors by

$$\mathbf{u}_i^1 = \frac{\int_{\mathcal{S}} \frac{1}{2} ((\partial_{\mathbf{t}_2} \phi_i)^2 - (\partial_{\mathbf{t}_1} \phi_i)^2) d\mathcal{S} + \lambda_i^1}{\int_{\mathcal{S}} -\partial_{\mathbf{t}_1} \phi_i \partial_{\mathbf{t}_2} \phi_i d\mathcal{S}} \mathbf{t}_1 + \mathbf{t}_2 \quad (\text{S2})$$

$$\mathbf{u}_i^2 = \frac{\int_{\mathcal{S}} \frac{1}{2} ((\partial_{\mathbf{t}_2} \phi_i)^2 - (\partial_{\mathbf{t}_1} \phi_i)^2) d\mathcal{S} + \lambda_i^2}{\int_{\mathcal{S}} -\partial_{\mathbf{t}_1} \phi_i \partial_{\mathbf{t}_2} \phi_i d\mathcal{S}} \mathbf{t}_1 + \mathbf{t}_2. \quad (\text{S3})$$

\mathbf{u}_i^1 is the eigenvector pointing in the direction of largest elongation and \mathbf{u}_i^2 is the one pointing in the direction of largest contraction of cell i . The director field is thus defined as $\mathbf{d}_i = \mathbf{u}_i^1 / \|\mathbf{u}_i^1\|$.

To take the periodicity of the domain into account when calculating the center of mass we follow the approach suggested in [S2].

Using that \mathbf{B} has an orthonormal basis out of eigenvectors and that the eigenvectors of \mathbf{B} are the principal curvature directions $\mathbf{t}_1, \mathbf{t}_2$ (with the values of principal curvature k_1, k_2 as eigenvalues) and the surface normal $\boldsymbol{\nu}$ with eigenvalue 0.0 we can rewrite the extrinsic curvature terms as

$$\langle \boldsymbol{\nu} \otimes \mathbf{B} \mathbf{d}_i, \boldsymbol{\nu} \otimes \mathbf{B} \mathbf{d}_i \rangle = k_1^2 \langle \mathbf{t}_1, \mathbf{d}_i \rangle^2 + k_2^2 \langle \mathbf{t}_2, \mathbf{d}_i \rangle^2 = \frac{1}{r_{Cyl}^2} \langle \mathbf{t}_1, \mathbf{d}_i \rangle^2, \quad (\text{S4})$$

where the last simplification holds only for a cylinder with radius r_{Cyl} since $k_2 = 0$ and $k_1 = \frac{1}{r_{Cyl}}$. In our setup for a cylinder the direction of the zero curvature is always aligned with the z -axis. Therefore the direction of the non-zero curvature is $\mathbf{t}_1 = \boldsymbol{\nu} \times \mathbf{e}_z$. In this setting, F_{EC} simplifies to

$$F_{EC} = Ec \sum_{i=1}^N \int_{\mathcal{S}} \langle \boldsymbol{\nu} \otimes \mathbf{B} \nabla_{\mathcal{S}} \phi_i, \boldsymbol{\nu} \otimes \mathbf{B} \nabla_{\mathcal{S}} \phi_i \rangle d\mathcal{S} = Ec \sum_{i=1}^N \int_{\mathcal{S}} \frac{1}{r_{Cyl}^2} \langle \nabla_{\mathcal{S}} \phi_i, \mathbf{t}_1 \rangle^2 d\mathcal{S}. \quad (\text{S5})$$

On a torus the directions and values of the principal curvature depend on the position $\mathbf{x} = (x_1, x_2, x_3)^T$. Therefore

eq. (S4) on the torus reads

$$\begin{aligned} \langle \boldsymbol{\nu} \otimes \mathbf{B}\mathbf{d}_i, \boldsymbol{\nu} \otimes \mathbf{B}\mathbf{d}_i \rangle &= k_1(\mathbf{x})^2 \langle \mathbf{t}_1(\mathbf{x}), \mathbf{d}_i \rangle^2 + k_2(\mathbf{x})^2 \langle \mathbf{t}_2(\mathbf{x}), \mathbf{d}_i \rangle^2 \\ &= \left(\frac{\sqrt{x_1^2 + x_2^2} - R_T}{r_T} \right)^2 \left\langle \begin{pmatrix} -x_2 \\ x_1 \\ 0.0 \end{pmatrix}, \mathbf{d}_i \right\rangle^2 + \frac{1}{r_T^2} \langle \boldsymbol{\nu}(\mathbf{x}) \times \mathbf{t}_1(\mathbf{x}), \mathbf{d}_i \rangle^2, \end{aligned}$$

and therefore we obtain

$$\begin{aligned} F_{EC} &= Ec \sum_{i=1}^N \int_{\mathcal{S}} \langle \boldsymbol{\nu} \otimes \mathbf{B}\nabla_S \phi_i, \boldsymbol{\nu} \otimes \mathbf{B}\nabla_S \phi_i \rangle d\mathcal{S} \\ &= Ec \sum_{i=1}^N \int_{\mathcal{S}} \left(\frac{\sqrt{x_1^2 + x_2^2} - R_T}{r_T} \right)^2 \left\langle \begin{pmatrix} -x_2 \\ x_1 \\ 0.0 \end{pmatrix}, \nabla_S \phi_i \right\rangle^2 + \frac{1}{r_T^2} \langle \boldsymbol{\nu}(\mathbf{x}) \times \mathbf{t}_1(\mathbf{x}), \nabla_S \phi_i \rangle^2 d\mathcal{S}. \end{aligned}$$

The sign of Ec determines whether the direction of largest elongation or the direction of largest contraction of the cell wants to align with the direction of largest absolute curvature. On a cylinder $Ec > 0$ leads to an elongation of the cells in azimuthal direction (green cell in Figure 1b) in the main article) and $Ec < 0$ leads to an elongation of the cell in longitudinal direction (yellow cell in Figure 1b) in the main article). On the torus the effect of Ec is less pronounced because the intrinsic curvature effects are much stronger. They determine the evolution and shape of the cell. The energy depends on the position of the cell and the geometry of the torus (as sketched in Figure 1c) in the main article).

Besides active driving in the direction of cell elongation we also consider a random model. This was sufficient to obtain collective rotation on the sphere [S6]. However, it turns out that this mechanism does not lead to coordinated movement on a cylindrical shape, see Figure S7. Instead of the elongation model with \mathbf{e}_1^i pointing in the direction of largest elongation, we specify \mathbf{e}_1^i to be the direction of movement from the previous time step. Such an approach was introduced in [S8] and can be considered as an extension of active Brownian particles to deformable objects. However, as already seen in [S13], where different propulsion mechanisms are compared, such an approach is not sufficient to resample basic mechanical properties. The numerical approach can be easily adapted to consider this propulsion mechanism.

CONSIDERED PARAMETERS

Table I summarizes the parameters varied in the simulations. The remaining parameters are kept constant during all simulations and are denoted in Table II. All cells are of equal size. All simulations correspond to an area fraction of 90%.

Ec	(r_{Cyl}, h_{Cyl})	(R_T, r_T)	activity mode
$-4.1 \cdot 10^{-6}, 0.0, 4.1 \cdot 10^{-6}$	$(0.41, 9.49), (0.60, 6.32), (1.51, 2.53)$	$(1.81, 0.81), (1.35, 1.08)$	elongation, random

Table I. Varied parameters for cylindrical and toroidal surfaces.

N_{Cyl}	N_T	ϵ	Ca	In	\tilde{a}_{rep}	\tilde{a}_{adh}	v_0	τ_n	D_r
60	144	0.01	10.0	0.05	0.0625	0.03	0.2	0.01	0.00045

Table II. Parameters used in all simulations.

DATA ANALYSIS

The data is evaluated after an initial time period so that our measurements are independent of the random initialization. The kymographs and averaged cell velocities over time in Figure 2 in the main article and in Figures S6

and S8 show one simulation in the time interval [50, 150]. The statistical data on the distribution of the direction of motion and elongation direction in Figures 3 and 4 in the main article and Figure S7 takes three different simulations into account.

For the polar plots of the cylinder showing the direction of movement (see Figure 3*a*) - 3*i*) in the main article and Figure S7*a*) - S7*i*) the velocity vectors \mathbf{v}_{cell} are calculated from the difference in \mathbb{R}^3 between the center of mass of the corresponding cell at time t and time $t + 6.0$. If the magnitude of the velocity vector is smaller than 10^{-6} it is not regarded, because we only want to consider velocity vectors where the movement direction surely dominates approximation errors, e.g. resulting from the approximate calculation of the center of mass. With this we have roughly 1500 data points for each plot.

We then calculate the angle between \mathbf{v}_{cell} and the longitudinal direction and compute the distribution from this. For the distribution we use 16 bins, so we divide the interval from 0° to 90° into 16 equal-sized bins. For each bin we calculate the mean velocity $\frac{\|\mathbf{v}_{\text{cell}}\|}{\|\mathbf{v}_{\text{cell}}\|}$ which is color-coded.

For the polar plots of the cylinder which show the distribution of the elongation direction (see Figure 3*j*) - 3*r*) in the main article and Figure S7*j*) - S7*r*) the elongation directions \mathbf{u}_i^1 have been calculated during run time according to eq. (2). We only consider values every 6 time units to be consistent with the evaluations for the direction of movement. Again we calculate the angle between \mathbf{u}_i^1 and the longitudinal direction and compute the distribution from this. For the distribution we use 16 bins, so we divide the interval from 0° to 90° into 16 equal-sized bins.

For the kymographs (Figure 2*b*) in the main article and Figures S6 and S8) the velocity in longitudinal (respectively azimuthal) direction of each cell is calculated. We calculate this from the center of mass of the corresponding cell at time t and time $t + 1.5$. The velocity in the azimuthal direction is calculated from the signed angle between (x_1, x_2) at the two time points and r_{Cyl} . For the azimuthal velocity the data points at each time point are sorted according to the height of the cell on the cylinder, i.e. according to x_3 of the center of mass of the cell. This makes also batch-wise rotation visible, e.g. all cells in the upper half of the cylinder rotating in one direction and all cell in the lower part of the cylinder rotating in the other direction. The longitudinal velocity is calculated from the difference of the x_3 -coordinates at the two time points. For the longitudinal velocity the data points at each time point are sorted according to the angle between (x_1, x_2) of the center of mass of the cell and the direction (1.0, 0.0). This makes also common movements in longitudinal direction of only a part of the cells visible.

The calculation of the polar plots (see Figure 4*a*)-4*f*) in the main article) for the tori, which show the direction of movement, is done similarly to the calculation of the polar plots for the cylinders except for two things: First, we calculate the velocity vectors \mathbf{v}_{cell} from the difference in \mathbb{R}^3 between the center of mass of the corresponding cell at time t and time $t + 1.5$, since the difference between the velocity vector in \mathbb{R}^3 and the velocity vector on the surface is larger for the tori than for the cylinder. Second, we calculate the angle between \mathbf{v}_{cell} and the poloidal direction instead of the angle with the longitudinal direction. For this we take the poloidal direction at the center of mass of the cell at $t + 0.75$. To be consistent with the plots for the direction of movement also for the polar plots showing the direction of elongation (see Figure 4*g*)-4*l*) in the main article) the values of \mathbf{u}_i^1 every 1.5 time units are used. There the angle between \mathbf{u}_i^1 and the poloidal direction is calculated with the poloidal direction at the center of mass at the same point in time.

The mean Gaussian curvature experienced by a cell, K_{cell} , is calculated at runtime using the following formulae:

$$K_{\text{cell}} = \frac{\int_{\mathcal{S}} K \psi_i d\mathcal{S}}{\int_{\mathcal{S}} \psi_i d\mathcal{S}} \quad (\text{S6})$$

with $\psi_i = \frac{1}{2}(\phi_i + 1)$. To evaluate the direction of movement with respect to K_{cell} (see Figure 4*m*) in the main text) we compute \mathbf{v}_{cell} and the angle with the poloidal direction exactly as for the polar plots. But this time the bins for the distribution are computed with respect to K_{cell} , where we took K_{cell} at $t + 0.75$. We used 10 bins, which are equally distributed between $K_{\text{cell}} = -3.26$ and $K_{\text{cell}} = 0.47$ as this where the minimal and maximal value for K_{cell} encountered in the simulations. In these bins the mean angle was calculated.

For the evaluation of the elongation direction in terms of K_{cell} (see Figure 4*n*) in the main text) the angles between the elongation direction and the poloidal direction are computed exactly as in the polar plots and the values of K_{cell} are taken from the same time step. As for Figure 4*m*) from the main text, the bins for the distribution are computed with respect to K_{cell} and 10 equally sized bins from $K_{\text{cell}} = -3.26$ to $K_{\text{cell}} = 0.47$ are used. In these bins the mean angle was calculated. The error bars in Figure 4*m*) and 4*n*) in the main article have the length of the standard deviation of the values in that particular bin.

RESULTS FOR A SINGLE CELL

The evolution of the energy for a single cell corresponding to Figure 1 in the main article is shown in Figure S4 for the cylindrical surfaces and in Figure S5 for the toroidal surfaces.

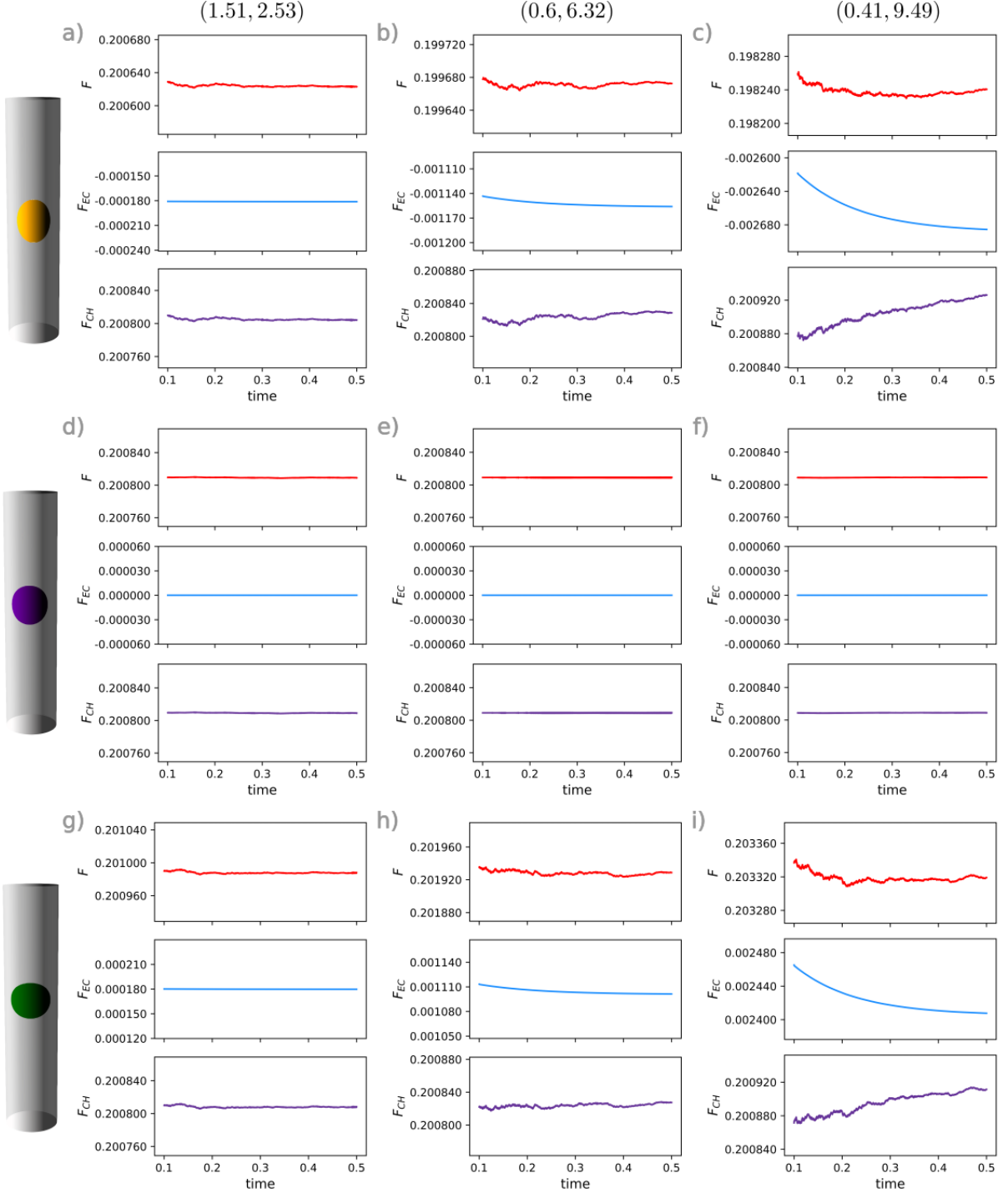


Figure S4. Time evolution of $F = F_{CH} + F_{EC}$, F_{CH} and F_{EC} for different cylindrical surfaces and different contributions of the extrinsic curvature energy. The different rows correspond to the extrinsic curvature contribution $Ec < 0$, $Ec = 0$ and $Ec > 0$ from top to bottom. The columns show the different cylindrical surfaces (r_{Cyl} , h_{Cyl}).

We consider the energy contributions F_{CH} and F_{EC} and $F = F_{CH} + F_{EC}$. We solve the evolution equation eq. (1)

in the main articles with $v_0 = 0$.

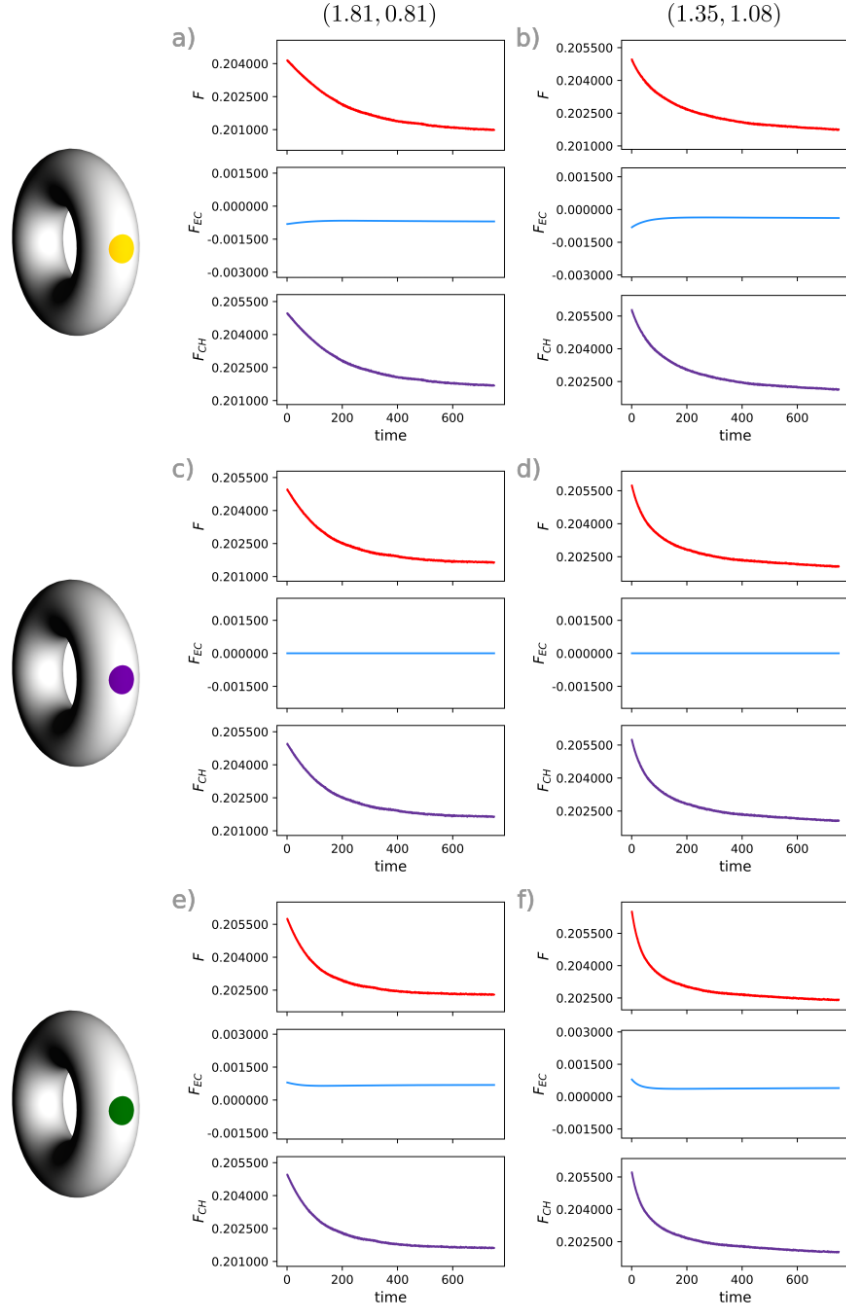


Figure S5. Time evolution of $F = F_{CH} + F_{EC}$, F_{CH} and F_{EC} for different toroidal surfaces and different contributions of the extrinsic curvature energy. The different rows correspond to the extrinsic curvature contribution $Ec < 0$, $Ec = 0$ and $Ec > 0$ from top to bottom. The columns show the different toroidal surfaces (R_T, r_T).

For the evaluation of one cell on the cylinder (see figure S4) we start with a geodesic circle on the cylinder, so the optimal solution for a system with $Ec = 0.0$. This is also illustrated by the Figures S4 d)-f), where no change in energy occurs because the solution is already optimal. If $Ec \neq 0.0$ a small deformation of the cell can lead to a further decrease of the total energy, since the geodesic circle is no longer the optimal solution. This effect is most visible for the cylinder with the highest curvature, see Figures S4 c) and S4 i). Decreasing F_{EC} is associated with an increase of F_{CH} . The sum of both energy contributions decreases. However, the absolute values of the energy contributions differ by three orders of magnitude.

For the toroidal surfaces the cell is placed on the inside of the torus. This leads to a movement of the cell towards

the outside of the torus. It is clearly visible that this is driven by F_{CH} and not F_{EC} , see Figure S5. The decrease of F_{CH} is by several orders of magnitude larger than changes in F_{EC} .

RESULTS FOR COORDINATED MOVEMENT

We provide the corresponding detailed data as shown in Figure 2 of the main article for all configurations considered in Figure 3 of the main article, see Figure S6. The results confirm the argumentation in the main article.

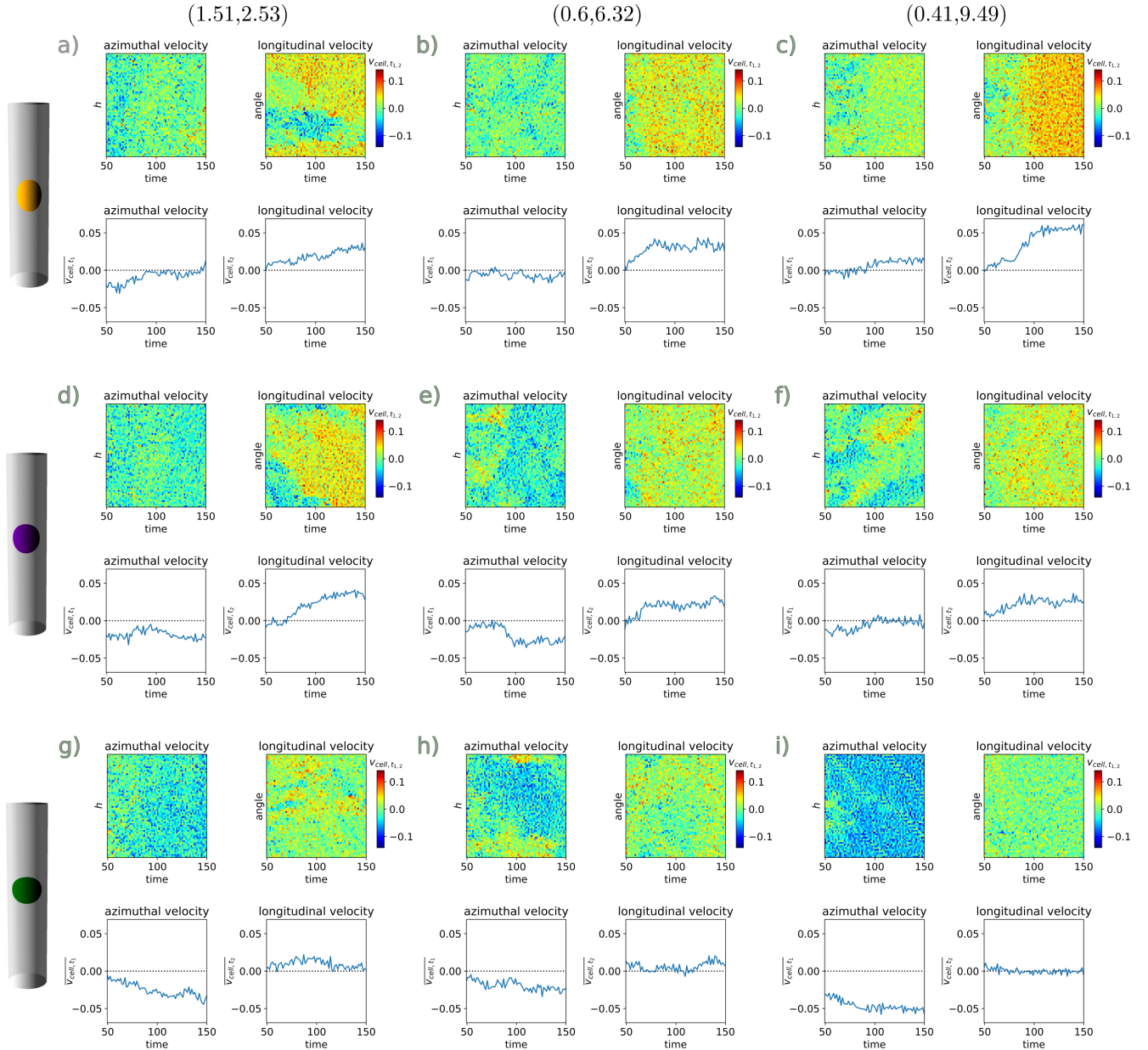


Figure S6. Kymographs and mean azimuthal/longitudinal velocity for the elongation model on cylindrical surfaces. The different rows correspond to the extrinsic curvature contribution $Ec < 0$, $Ec = 0$ and $Ec > 0$ from top to bottom. The columns show the different cylinders (r_{Cyl}, h_{Cyl}) with increasing curvature from left to right.

In addition we provide the corresponding results for a random propulsion mechanism, see figures S7 and S8. While a preferred elongation direction depending on Ec is visible for the cylinder with the largest curvature, there is no preferred direction of movement.

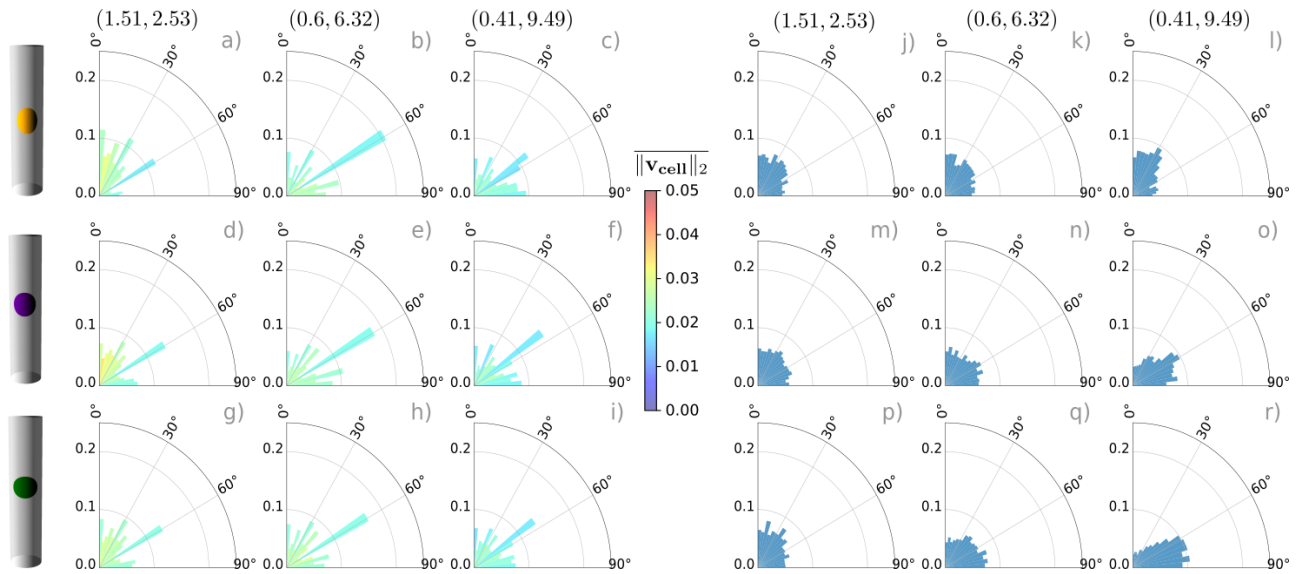


Figure S7. Distribution of direction of motion (left) and elongation direction (right) for the random model on cylindrical surfaces. The different rows correspond to the extrinsic curvature contribution $E_c < 0$, $E_c = 0$ and $E_c > 0$ from top to bottom. The columns show the different cylinders (r_{Cyl}, h_{Cyl}) with increasing curvature from left to right. The angle between \mathbf{e}_3 and the direction of movement or elongation direction is used as the angular coordinate and the ratio of cells with this property as the radial coordinate. *a*)-*i*) show the direction of movement with color-coding the mean velocity, *j*)-*r*) show the direction of elongation.

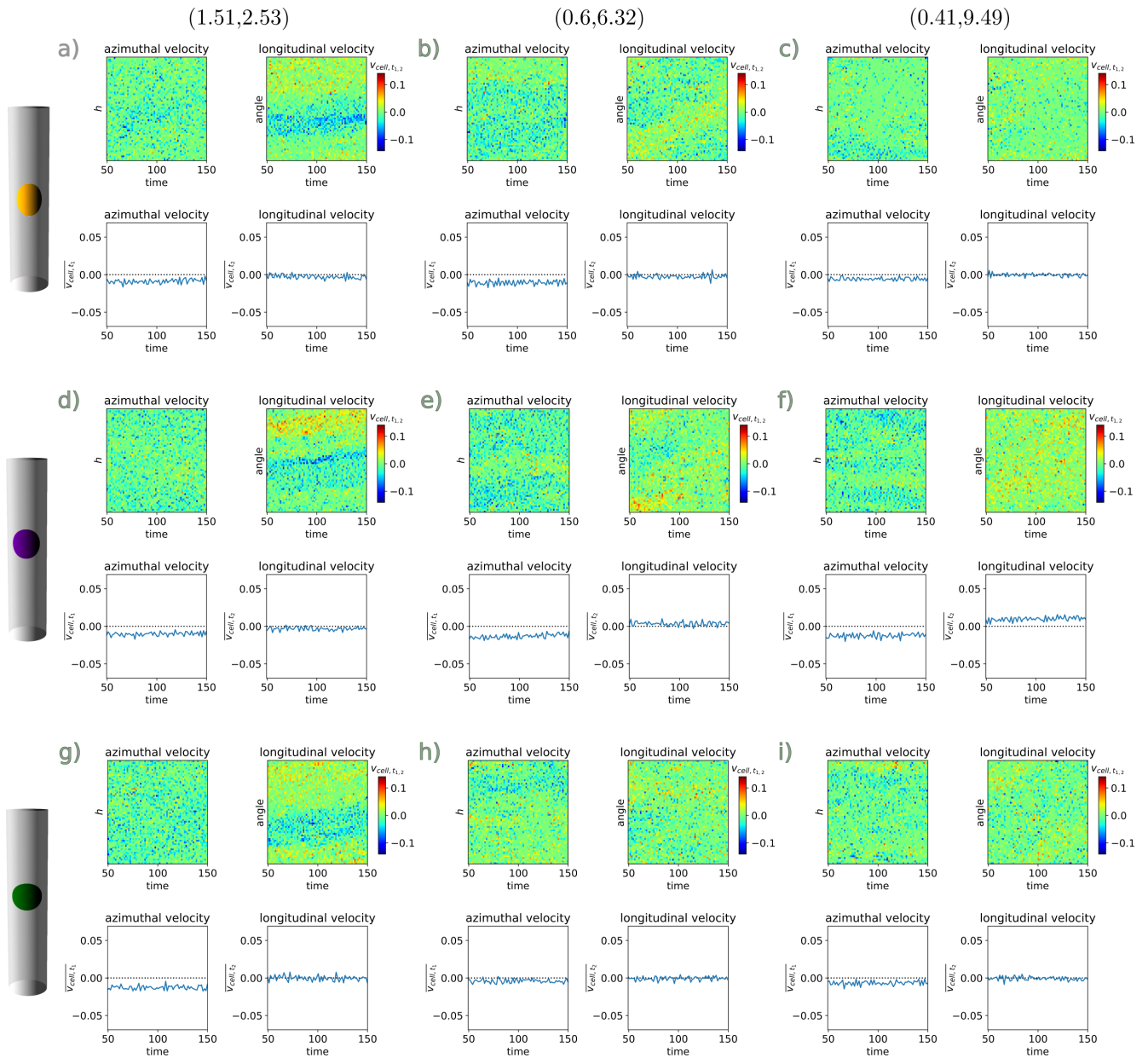


Figure S8. Kymographs and mean azimuthal/longitudinal velocity for the random model on cylindrical surfaces. The different rows correspond to the extrinsic curvature contribution $Ec < 0$, $Ec = 0$ and $Ec > 0$ from top to bottom. The columns show the different cylinders (r_{Cyl}, h_{Cyl}) with increasing curvature from left to right.

MOVIES

We provide movies for the considered geometries with $Ec > 0$, modeling the behaviour of MDCK cells, corresponding to Figure 3 g), h), i) or p), q), r) in the main article for the cylindrical surfaces and Figure 4 e), f) or k), l) in the main article for the toroidal surfaces. The movies show one simulation within the time frame $[50, 150]$. The cells are visualized by their zero level sets $\phi_i = 0$.

-
- [S1] E. Bachini, V. Krause, I. Nitschke, and A. Voigt. Derivation and simulation of a two-phase fluid deformable surface model. *arXiv:2305.15147*, 2023.
 - [S2] L. Bai and D. Breen. Calculating center of mass in an unbounded 2D environment. *J. Graphics Tools*, 13(4):53–60, 2008.
 - [S3] P. Bastian, M. Blatt, A. Dedner, N.-A. Dreier, C. Engwer, R. Fritze, C. Gräser, C. Grüniger, D. Kempf, R. Klöforn, M. Ohlberger, and O. Sander. The Dune framework: Basic concepts and recent developments. *Computers & Mathematics with Applications*, 81:75–112, 2021.
 - [S4] P. Brandner, T. Jankuhn, S. Praetorius, A. Reusken, and A. Voigt. Finite element discretization methods for velocity-pressure and stream function formulations of surface Stokes equations. *SIAM J. Sci. Comput.*, 44:A1807–A1832, 2022.
 - [S5] G. Dziuk and C. M. Elliott. Finite element methods for surface PDEs. *Acta Numerica*, 22:289–396, 2013.
 - [S6] L. Happel, D. Wenzel, and A. Voigt. Effects of curvature on epithelial tissue - coordinated rotational movement and other spatiotemporal arrangements. *Europhys. Lett.*, 138:67002, 2022.
 - [S7] V. Krause and A. Voigt. A numerical approach for fluid deformable surfaces with conserved enclosed volume. *J. Comput. Phys.*, 486:112097, 2023.
 - [S8] B. Loewe, M. Chiang, D. Marenduzzo, and M. C. Marchetti. Solid-liquid transition of deformable and overlapping active particles. *Phys. Rev. Lett.*, 125:038003, 2020.
 - [S9] M. Nestler, I. Nitschke, and A. Voigt. A finite element approach for vector-and tensor-valued surface PDEs. *J. Comput. Phys.*, 389:48–61, 2019.
 - [S10] S. Praetorius and F. Stenger. Dune-CurvedGrid - A Dune module for surface parametrization. *Archive of Numerical Software*, 6:1–27, 2022.
 - [S11] S. Praetorius and A. Voigt. Collective cell behavior - a cell-based parallelization approach for a phase field active polar gel model. In K. Binder, M. Müller, and A. Trautmann, editors, *NIC Symposium 2018*, volume 49, pages 369–376, Jülich, 2018. Forschungszentrum Jülich GmbH, Zentralbibliothek.
 - [S12] S. Vey and A. Voigt. AMDiS: Adaptive multidimensional simulations. *Comput. Vis. Sci.*, 10:57–67, 2007.
 - [S13] D. Wenzel and A. Voigt. Multiphase field models for collective cell migration. *Phys. Rev. E*, 184:054410, 2021.
 - [S14] T. Witkowski, S. Ling, S. Praetorius, and A. Voigt. Software concepts and numerical algorithms for a scalable adaptive parallel finite element method. *Adv. Comput. Math.*, 41:1145–1177, 2015.